Analyst

Surface Dependent Enhancement in Water Vapor Permeation through Nanochannels

Journal:	*Analyst*
Manuscript ID	AN-ART-04-2018-000650.R1
Article Type:	Paper
Date Submitted by the Author:	26-Jun-2018
Complete List of Authors:	Rangharajan, Kaushik Krishna; The Ohio State University, Mohanasundaram, Prashanth; The Ohio State University Conlisk, A.T.; The Ohio State University, Prakash, Shaurya; The Ohio State University, Department of Mechanical Engineering

Surface Dependent Enhancement in Water Vapor Permeation through Nanochannels

Kaushik K. Rangharajan, Prashanth Mohanasundaram, A.T. Conlisk, Shaurya Prakash*

Department of Mechanical and Aerospace Engineering, The Ohio State University, Columbus, OH 43210, USA

*Corresponding Author: prakash.31@osu.edu

Abstract

Selective permeation of water vapor over liquid phase water through hydrophobic conduits finds broad use in separation processes, including desalination and membrane distillation. The tangential momentum accommodation coefficient (TMAC), a fundamental parameter that dictates momentum changes to a molecule colliding with a wall remains unknown for water vapor at room temperature and pressure conditions. Here, a nanofluidic platform with tunable hydrophobic regions that selectively barricaded flow of liquid water was patterned within glass nanochannels. The surface functionalization with an alkyltrichlorosilane led to either a fluoride or a methyl terminal group generating partially hydrophobic regions along the length of the nanochannels. Differential osmotic pressure solutions on either side of the hydrophobic region cause an isothermal evaporation-condensation process, which drives net water vapor transport from higher to lower vapor pressure solution, similar to osmotic distillation. Water vapor transport under such conditions for the 80 nm deep nanochannels was in the transitional regime with the Knudsen number ~O(1). The TMAC was estimated experimentally to be of the order of 10^{-4} – 10^{-3} for both the hydrophobic coatings leading to a near-elastic collision of H_2O molecules with the nanochannel walls. Use of the low TMAC surfaces was evaluated in two proof-of-concept technology demonstrations: (1) osmotic distillation using hyper-saline (brine) 3 M Utica shale flowback water as both the feed and draw and (2) separation of trace amounts of toluene and chloroform from water at high flux and selectivity. The results reported here likely provide new insights in designing hydrophilic-hydrophobic junctions for nanoscale liquid/vapor fluid transport with enhanced flux and selectivity.

Introduction

Liquid-vapor transport is a critical domain for nanoscale transport[1] with applications in antifouling surfaces,[2] water desalination,[3] food storage,[4] wearable electronics,[5] microfluidics,[6] energy generation,[7] and a variety of separations including those driven by hydrophobic membranes[8-9] and emerging materials (e.g., zeolites).[10-11] Overall mass transport in a liquid-vapor or similar two-phase flow systems is governed by resistance to flow during transmission i.e., momentum losses due to molecule-molecule or molecule-wall collisions[12] and resistance at the liquid-vapor interface.[13] In recent years, nanoscale conduits or nanofluidic architectures have been widely investigated for wall-fluid interactions leading to advances in the understanding of surface charge mediating aqueous electrolyte flows,[14] modeling, and measurement of evaporation-condensation coefficients,[13] large slip for unusually high permeate flux,[15-16] and evaluation of kinetic mass-transfer limits for evaporation.[17-18] Despite this increasing body of work, a systematic evaluation of transmission resistance in nanofluidics for liquid-vapor systems remains largely unexplored.

Transmission of vapor through sub-100 nm spaces with critical dimension h, at atmospheric pressures (e.g., applications in pervaporation and membrane distillation processes) is indicative of non-continuous or transitional flow, since the mean free path λ, at atmospheric pressure (60 – 80 nm)[13] is comparable to the confinement or critical device length scale, and the Knudsen number Kn (λ/h) is ~ O(1). When Kn is ~ O(1) the transmission resistance to flow arises primarily due to momentum changes from the fluid molecule collisions with the physical nanochannel wall as opposed to molecule-molecule collisions. The fluid molecule collisions with the physical walls are typically quantified by the tangential momentum accommodation coefficient (TMAC with the symbolic notation σ_v), which arises from the correction to the no-slip flow condition at the physical wall.[19] Furthermore, the first discussions for TMAC follow from the work by Maxwell[20] capturing two limiting cases for fluid-wall collisions: (**1**) The case of specular reflection, where $\sigma_v = 0$, signifying the tangential velocity of the molecule reflected from the wall upon collision remains unchanged i.e., a perfectly elastic collision preserving momentum in the direction of travel (or, ideal flows with perfect slip and no transmission resistance) and (**2**) the case of diffuse reflection ($\sigma_v = 1$), where the tangential velocity of the molecule becomes zero after reflection from the wall as a result of a perfectly inelastic collision.[12, 21]

Previous studies report the importance of specific surface type and surface roughness in influencing the TMAC of noble gas collisions, where and a lower TMAC was measured for nobles gas

collisions with atomically smooth surfaces (e.g., silver, titanium) as opposed to rough surfaces (titanium coated with oxygen).[22] TMAC values have been reported for many gas flows (usually ideal, inert gases like N_2 or Ar) with values usually ranging from 0.2 – 1 with functional dependence on the gas molecule, *Kn*, and properties of the colliding wall surface.[12, 21-24] Moreover, several reports for similar gases and surface systems have reported significantly different σ_v.[12, 22-23] Recent experiments (for $Kn \sim O(1)$) with water vapor reveal that the predicted Hertz-Knudsen equation break down at the nanoscale and the measured flux was higher by more than an order of magnitude.[18] However, the literature lacks clarity on specific surface-mediated transport mechanisms and adequate theoretical models and explanations. Notably, σ_v has not been reported for water vapor at atmospheric pressure conditions for any surface despite extensive literature on gas flows in microchannels.[12, 21-24]

The purpose of this paper is to report on the tangential momentum accommodation coefficient for water vapor using systematic flux measurements aided by advanced gas flow and slip models[19] at atmospheric pressure and room temperature. Specifically, in order to report the first reliable value of σ_v for water vapor under ambient conditions for a nanoscale conduit, a model silica-based nanofluidic platform with well-defined geometries was developed facilitating visualization of an engineered two-phase flow driven by an evaporation-condensation process. Furthermore, partial hydrophobic regions of tunable length varying from 96 μm – 595 μm were functionalized within the hydrophilic silica nanochannels using diffusion-limited patterning[25] for quantifiable measurements of water vapor transport between liquid/vapor interfaces. Additionally, nanoscale water vapor flux and σ_v due to specific terminal functional groups (fluoride and methyl) on the silica walls were determined thereby accounting for differences in bulk contact angle (and related surface chemistry) on net flux. Additionally, the net flux of the nanofluidic platform under varying magnitude of osmotic pressure and hydrophobic lengths for a given surface is subsequently described. Finally, the viability of liquid-vapor systems for desalination of brines from shale flowback water and separation of trace amounts of volatile organics from water are demonstrated as potential applications enabled by surfaces within nanofluidic channels that exhibit negligible transmission resistance.

Results and Discussion

Fabrication of model nanofluidic device

Our team has previously reported on design and fabrication of the nanofluidic platform.[14, 26] Briefly, the model silica-based nanofluidic device architecture consists of two parallel microfluidic channels connected *via* three parallel nanofluidic channels (80 nm high x 30 μm

wide x 2.5 mm long; Figure 1a and Figure 1a inset) oriented perpendicular to the microchannels (8 µm high x 50 µm wide x 3 cm long). The critical dimension for the nanochannel depth was chosen to be 80 nm in order to have transport occur in the $Kn \sim 1$ regime to evaluate explicitly the impact of surface modification on the transmission resistance across the nanochannel.

Nanochannel surface modification

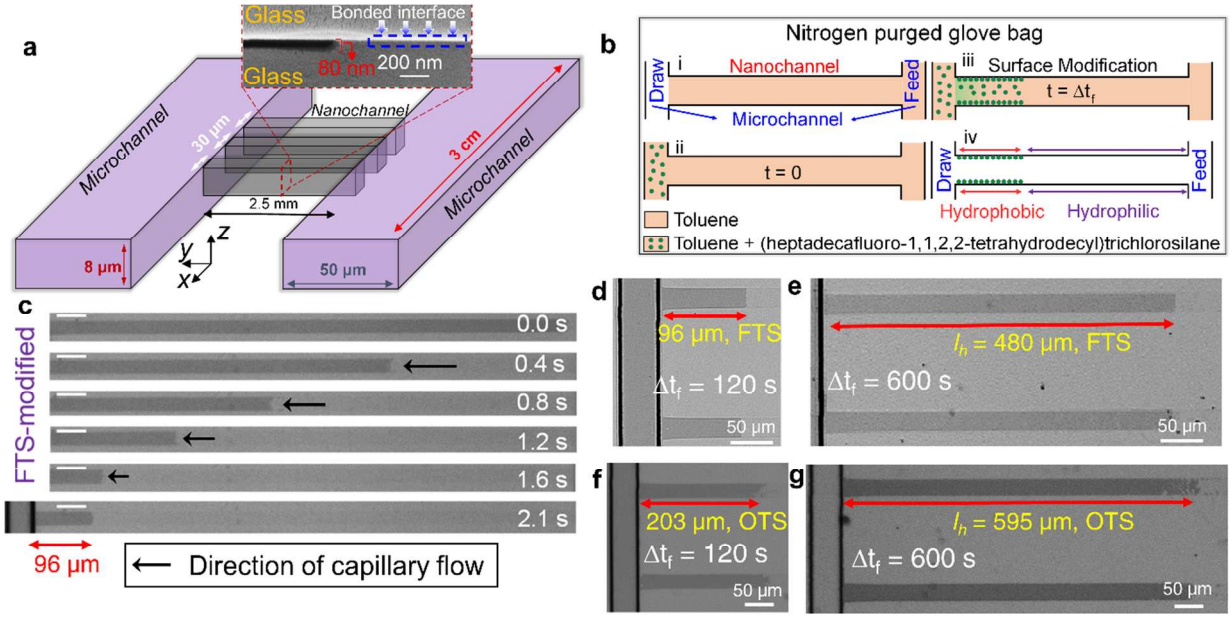

Figure 1: ***(a)*** *Schematic shows device layout for the proof-of-concept device consisting of two microchannels (8 µm deep x 50 µm wide and 3 cm long) that serve as fluidic reservoirs for three nanochannels (80 nm deep x 30 µm wide x 2.5 mm long). Inset shows a scanning electron microscope (SEM) image of the partial nanochannel cross-section and the bonded glass-glass interface.* ***(b)*** *Schematic of the sequential surface modification process (i – iv) to pattern finite length hydrophobic regions inside the nanochannel as discussed in the main text. Time-lapse images showing capillary filling of de-ionized (DI) water in* ***(c)*** *FTS-modified nanochannel where capillary induced flow stops at a distance of 96 µm from the draw microchannel. Scale bars are 50 µm.* ***(d)*** *By controlling* Δt_f *(as described in main text), hydrophobic regions of* l_h *= 96 µm, and* ***(e)*** *480 µm were patterned using FTS, and* ***(f)*** l_h *= 203 µm and* ***(g)*** l_h *= 595 µm were patterned using OTS.* l_h *denotes the length of the vapor trap.*

To obtain partial hydrophobic sections inside the nanochannels, diffusion limited patterning was used.[25] Briefly, 100% anhydrous toluene was released from the feed access point (Figure 1b(i)), with capillary action drawing the anhydrous toluene into the microchannel and nanochannel. Next, the stock functionalization solution for either heptadecafluoro-1,1,2,2-

tetrahydrodecyl)trichlorosilane (FTS, fluoride terminal group) or n-Octadecyltrichlorosilane (OTS, methyl terminal group) was introduced into draw access point (Figure 1b(ii)), which fills the draw microchannel also due to capillary action. Regulation of the total residence time Δt_f (120 s to 600 s) of the stock functionalization solution governs the total available diffusion time for the silane from the stock solution to diffuse into the nanochannel, and render a finite length of the surface hydrophobic (Figure 1b(iii)).

While a concentration gradient in silane likely exists in the bulk of the nanochannel during the during the surface modification process (Figure 1 b(iii)), past reports[27-29] have shown that post-formation of the monolayer, followed by copious flushing removes any additional physisorbed surface layers and the degree of non-uniformity, if any, is unlikely to impact the operation of the nanochannels. After Δt_f has elapsed, all the solvents were pumped out (Figure 1b(iv)).

Estimation of vapor-trap length (l_h)

The exact length of the patterned hydrophobic region (Figure 1b(iv)) was estimated by introducing DI water through the unmodified feed microchannel. The use of glass permits direct visualization of the liquid-vapor interface when the meniscus encounters the hydrophobic regions to halt the capillary driven flow. Capillary action driven by surface tension pulled the water inside the feed microchannel and also subsequently inside the nanochannels,[30] which was captured using a Nikon inverted series-Eclipse microscope at 12.5 frames/second (Figure 1c). Surface tension driven capillary filling of water in hydrophilic silica nanochannels is well studied[30] and the filling dynamics here conform to the predictions from Lucas-Washburn equations (Figure S1). In contrast to the hydrophilic silica nanochannels, the dynamics of capillary filling change significantly as the water meniscus transitions from the hydrophilic to hydrophobic regions of the nanochannels (supplementary information S1).

Resulting changes to the filling velocity and filling time for the partially hydrophobic channels were also estimated from the microscope time-lapse images and are reported in the supporting information (Figure S1 – S2). In comparison to unmodified (i.e., hydrophilic) silica channels, the hydrophobic patches slow the progress of the water meniscus (Figure S2) and ultimately halt the capillary flow at a finite distance from the draw microchannel (Figure 1c, Supplementary Movie S1). The total distance between the draw microchannel and the stationary front of the water meniscus was defined as the vapor-trap length, l_h. By varying the duration of

surface modification process Δt_f, tunable sections of varying l_h were patterned (Figure 1d-g). For a fixed Δt_f = 120 s (2 min), a hydrophobic length of 96 μm (Figure 1d) and 203 μm (Figure 1f) were patterned using FTS and OTS respectively. Similarly, for a Δt_f = 600 s, a hydrophobic length of 480 μm (Figure 1e) and 595 μm (Figure 1g) were patterned using FTS and OTS respectively. The molecular weight of OTS (387.93 g, CAS No.: 112-04-9) is 33.3% less than FTS (581.56 g, CAS No.:78560-44-8) promoting faster diffusivity and longer l_h for a fixed Δt_f. The partial hydrophobic region (Figure 1d-g) showed no water infringement confirming viability of the hydrophobic region, referred to as a vapor trap in the remainder of this paper.

Prevention of water leakage inside vapor-traps

Figure 1d-g provided visual confirmation of a dry channel with no apparent water leakage across the vapor-trap. However, as with most nanofluidic platforms, additional methods may be required to verify that visual observations are indeed correct. Consequently, in a true vapor-trap, electrolyte conduction would be minimal i.e., the electrical resistance would be high since there is no direct path for charge transfer through the liquid phase. Electrical conductance[14] was measured across the vapor-trap by the application of potential difference between feed and draw, both filled with 0.1 M NaCl (Figure S3). Measured conductance over a duration of 20 min was nearly three orders of magnitude lower in device with vapor-traps in comparison to devices with no vapor-trap (unmodified devices) implying lack of electromigration of ions.

Vapor pressure driven transport of water molecules inside hydrophobic vapor-trap

Engineered vapor-traps of length l_h (Figure 2) when sandwiched by aqueous solutions of different vapor pressure permits net transport of water vapor from regions of higher vapor pressure (feed) to lower vapor pressure (draw). The water vapor transport across the vapor trap facilitates estimation of σ_v governing water vapor – hydrophobic surface collisions. Water vapor transport is driven by the isothermal evaporation and condensation of water vapor between the feed and draw and is initiated due to the osmotic pressure gradient[7, 13] across the vapor trap that prevents liquid water from crossing the hydrophobic barrier. The osmotic gradient is introduced by a lower concentration solution as feed in comparison to draw.[7, 13] During this osmotic distillation process, all non-volatile substances remain in the feed, presenting an ideal case for highly selective mass transport which has broad applications for separation in two-phase systems.[8, 10] Theoretically, the reduction in equilibrium vapor pressure of a salt solution with an osmotic pressure Π, compared to DI water is given by[13]

$$P_{vap} = P_{vap}^{0} e^{\frac{-\Pi V_m}{R_g T}} \quad . \tag{1}$$

Where, P_{vap}^{0} is the equilibrium vapor pressure of DI water at temperature T, V_m is the molar volume of pure water at temperature T, and R_g is universal gas constant. From previous molecular dynamic simulations the fugacity of saturated water vapor at 298K was approximately unity,[31] implying that the assumption of ideal equilibrium vapor pressure for water is valid.[31] Here, P_{vap}^{0} is 3.17 kPa and V_m is 1.8 x 10^{-5} m^3/mol based on previously published values.[7]

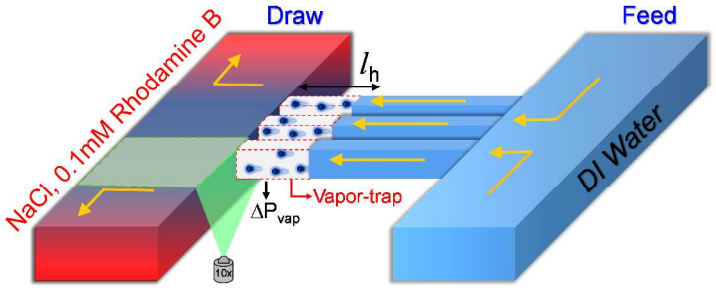

Figure 2: The schematic shows the basic principle behind osmotic distillation across the vapor trap. As a model fluid, DI (de-ionized) water was introduced as the feed and an aqueous NaCl solution (0.5 – 2 M) fluorescently tagged with Rhodamine B dye was introduced as the draw. The hydrophobic regions barricade flow of liquid water allowing for selective vapor-pressure driven water vapor transport from higher vapor pressure DI water feed compared to lower vapor pressure, saline water draw. Condensation of water vapor reduces the fluorescence intensity of Rhodamine B and was continuously imaged over 20 min for different vapor-trap lengths to determine optically the flux of water arriving at the draw from the feed.

The osmotic distillation system was initiated by introduction of DI water into the feed microchannel and aqueous NaCl solution (0.5 M – 2 M), tagged with 0.1 mM Rhodamine B dye (Rb) introduced into the draw microchannel. The chosen draw compositions mimic the range of salinities found from seawater to hypersaline (brine) solutions intended to mimic a variety of industrial water types. Condensation of water vapor on the draw side microchannel dilutes the NaCl draw solution containing the Rb dye (Figure 2). A drop in the Rb fluorescence intensity *($\lambda_{ex}/\lambda_{em}$ = 540/625 nm)* was monitored over a 100 µm x 50 µm window located at the microchannel-nanochannel junction for a duration of 20 minutes (Figure 2) with declining intensity implying the continued dilution of the draw solution. Visually, no condensation of water molecules was observed inside the vapor-trap during experiment. Separate calibration curves were

generated to correlate the reduction in dye intensity to reduction in salt concentration (Figure S4) to determine the flux of incoming water from the feed to the draw.

Unified slip model for σ_v determination

Here, with nanochannel depth at h = 80 nm, $Kn \sim 1$ at atmospheric pressure, implying that the water vapor transport follows the transitional flow regime across the vapor trap.[32] Fluid flows in transitional regimes ($0.1 < Kn < 10$)[32-33] are typically analyzed either by using *ad-hoc* empirical models or *via* Direct simulation Monte Carlo (DSMC) simulations.[34] In contrast to stochastic methods (e.g., DSMC), facile theoretical alternatives exists that incorporate fluid slip and rarefaction phenomenon in the Naiver-stokes equation[35] and have been validated against velocity profiles from DSMC simulations.[19, 32] Here one such model, namely unified slip model (USM) that employs Navier-Stokes equation with a O(Kn^2) correction for precise slip boundary was used. USM model has been previously validated experimentally for rarefied gas flows in rectangular nanochannel,[19, 32] and was implemented here to calculate the values of σ_v for water vapor transport through the hydrophobic vapor-trap from the measured experimental flux. The flux J_{nano}, for transitional flows in a nanochannel of height h, can be expressed as,

$$J_{nano} = \frac{\Delta P_{vap}(\xi+1)\, h^2 \rho_{wv}}{24\, l_h\, \mu_{wv}}\left[1 + 2\frac{\overline{\alpha} + 6\left(\frac{2-\sigma_v}{\sigma_v}\right)}{\xi+1} Kn + 12\frac{(\overline{\alpha}+b)}{\xi^2-1}\left(\frac{2-\sigma_v}{\sigma_v}\right)\log\left(\frac{\xi - b\, Kn}{1-b\, Kn}\right) Kn^2\right]. \quad (2)$$

Where, ΔP_{vap} is the vapor pressure difference between feed and draw driving water vapor transport for the vapor trap, ξ is the ratio of feed to draw vapor pressure, ρ_{wv}, μ_{wv} are the density and viscosity of water vapor respectively.[19, 32] b characterizes the second order O(Kn^2) correction to the no-slip boundary condition and is correlated from experimental studies to have a value of ~ -1.[19, 32] $\overline{\alpha}$ accounts for effect of walls on viscosity, and σ_v (TMAC) arises from O(Kn) correction to no-slip condition.[32]

Surface wettability dictates nanoscale water vapor flux

Estimation of the tangential momentum accommodation coefficient requires connecting a measurable flow quantity such as the flux of vapor transport to a phenomenologically based fluid slip model. Here both, J_{nano} and σ_v (Eq. 2) were estimated for water vapor transport through both heptadecafluoro-1,1,2,2-tetrahydrodecyl)trichlorosilane (FTS) or n-Octadecyltrichlorosilane (OTS) modified nanochannels. Error propagation analysis[36] accounts for measurement uncertainties associated with multiple measurements of flux for a given draw concentration, channel dimensions, and Kn.[13] While the USM has three non-dimensional parameters, namely, $\overline{\alpha}$

, b, and σ_v (TMAC) affecting net flux, sensitivity analysis (see supplementary information) showed that in contrast to the viscosity changes and the second order slip correction b, derivative of flux with σ_v was three orders of magnitude higher than the derivative of flux with $\overline{\alpha}$, b (Figure S5) indicating that σ_v is the dominating parameter for controlling J_{nano}. For the given experimental conditions in FTS-modified nanochannels, achieving a flux greater than 100 $g \cdot m^{-2} \cdot s^{-1}$ (Figure 3a) was possible only with a reduction in TMAC in contrast to changing $\overline{\alpha}$, b. Equation 2 was solved using a non-linear solver in Mathematica (Wolfram Research, v11.0) to calculate σ_v (Figure 3a) for each draw concentration and l_h, assuming $\overline{\alpha}$ = 2 and b = -1 from previous reports.[19, 32]

In FTS-modified channels, J_{nano} of 122.2 $g \cdot m^{-2} \cdot s^{-1}$ and 85.5 $g \cdot m^{-2} \cdot s^{-1}$ was estimated for l_h = 96 μm and 480 μm respectively for a draw concentration of 1 M (Π = 48 bar, Figure 3a). Similarly, for OTS-coated channels, the nanoscale water vapor flux for l_h = 203 μm was higher than water vapor flux through l_h = 595 μm by about 15% (Figure 3b). The TMAC for both FTS and OTS-coated nanochannels were ~$O(10^{-4})$ as calculated from equation 2 by using the values of J_{nano} measured from the dye dilution experiments (see methods). The σ_v values at $O(10^{-4})$ indicate specular reflection or near-elastic collision of water-vapor with the hydrophobic surfaces and decreased with increase in l_h. The reported average TMAC (Figure 3 c, d), quantifying the molecule-wall interaction for a given vapor-trap length l_h, was estimated from the measured flux. For a longer hydrophobic channel, the water molecules undergo more collisions with the channel walls from feed to the draw compared to shorter nanochannels, resulting in lower measured flux as reported in Figure 3. For a given surface chemistry (either the fluorinated surface (FTS) or the methylated surface (OTS)), in-addition to surface dependent molecule-wall interactions, previous molecular dynamic (MD) simulations[37] have shown that the TMAC of a given collision is also a function of the angle of incidence of a molecule with respect to a surface. A lower TMAC was reported when the angle of incidence (with respect to normal to the surface) was higher, signifying increased elasticity in collision.[37] From Figure 3 c, d it is observed that for a given surface, the average TMAC decreases with increase in l_h. It is also worth noting that the flux measurements of both FTS and OTS surfaces (Figure 3 a, b) do not show a linear decrease in flux with increase in $l_{h,}$ that is typically observed in continuum pressure driven flows.[19]

For the same osmotic pressure of 48 bar, OTS-modified channels exhibited higher flux of 94.4 $g \cdot m^{-2} \cdot s^{-1}$ for l_h = 595 μm (Figure 3b) in comparison to shorter FTS-modified channels with l_h = 480 μm (85.5 $g \cdot m^{-2} \cdot s^{-1}$). Higher TMAC for FTS-modified nanochannels (Figure 3c) in comparison to OTS-modified nanochannels (Figure 3d) likely suggests the contrasting role of negligible hydrogen bonding in CH_3-H_2O interactions (OTS channels) compared to fluorine as a

hydrogen bond acceptor in FTS-modified channels in dictating flux.[38] Moreover, past work on flat surfaces has also shown significantly higher drainage velocity for thin water films on methylated surfaces in contrast to other common surfaces.[39] The observed trends also agree with molecular dynamic simulations that show significant enhancement in water permeation in carbon nanotubes is destroyed in the presence of strong hydrogen bonding.[40]

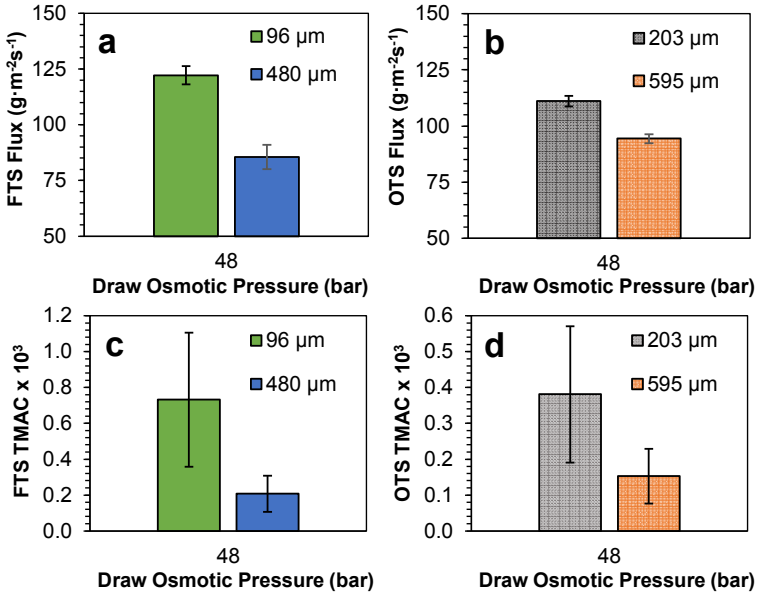

*Figure 3: For a fixed draw osmotic pressure of 48 bar, J_{nano} was measured for **(a)** FTS-coated and **(b)** OTS coated nanochannels. Equation 2 with the experimentally measured J_{nano} was used to calculate TMAC values from unified slip model for **(c)** FTS-coated and **(d)** OTS coated nanochannels. TMAC decreases with increases in length of vapor-trap for both FTS and OTS-coated nanochannels. Error bars represent ± standard deviation (s.d.) from the mean.*

Mechanistic interactions for FTS and OTS were also considered from differences in surface wettability as (**1**) OTS-modified glass has a higher contact angle (110° – 120°) [41-42] in comparison to FTS-modified glass (static contact angle of 105.3°).[36] Stronger water-surface interactions for relatively more wettable (FTS in contrast to OTS) channels[43] require higher activation energy, limiting the net flux and corresponds to a higher calculated σ_v. Conversely, interaction of water molecules with water-repelling surface at nano-confinement, reducing activation energy can enhance net flux.[44] Our past results also show a significant correlation between macroscopic contact angle and contact line pinning induced line tension at the solid-liquid-vapor interface, influencing droplet curvature at the nanoscale[36] and likely having direct implications for the net evaporation rate from the pinned meniscus.[45]

Variation of J_{nano} and σ_v with draw osmotic pressure for FTS-coated vapor-traps

Nanoscale water vapor flux and TMAC were estimated over a range of draw osmotic pressures from 24 bar (0.5 M) – 96 bar (2 M) for FTS-coated vapor-traps of l_h = 96 µm and 480 µm. In general, J_{nano} was ~O(10^1 – 10^2) g·m^{-2}·s^{-1} and increased with increase in draw osmotic pressure for both l_h = 96 µm and 480 µm due to an enhanced vapor pressure difference between feed and draw (Figure 4a). Over the tested draw concentrations, TMAC varied between 0.4 x 10^{-3} – 0.9 x 10^{-3} for l_h = 96 µm (Figure 4b) and between 0.1 x 10^{-3} – 0.3 x 10^{-3} for l_h = 480 µm (Figure 4c). One-way ANOVA followed by Tukey post-hoc honestly significant difference (HSD) test was conducted to quantify the statistical significance of TMAC values between any two pairs of draw compositions. p-value estimated from Tukey HSD test revealed statistically not significant (NS, p > 0.2) TMAC differences upon comparison of pair-wise means, estimated for draw osmotic pressure between 48 bar (1 M) and 96 bar (2 M) for both l_h = 96 and 480 µm. TMAC exhibited vapor pressure dependence (Figure 4 b, c) only when draw concentrations was less than 1 M.

The range of low values for TMAC reported here suggests that interaction of water vapor molecules with FTS-modified nanochannels walls approaches near-elastic collision and can be classified as specular reflection. A perfectly elastic collision (TMAC = 0), is representative of an ideal system and would be thermodynamically possible when no entropy changes (adiabatic-reversible process) are involved with molecule-wall collisions. Such a system may be impossible to physically implement and therefore for any practical system as $\sigma_v \rightarrow 0$, the transmission resistance becomes negligible providing high flux for a given geometry of the nanochannel.

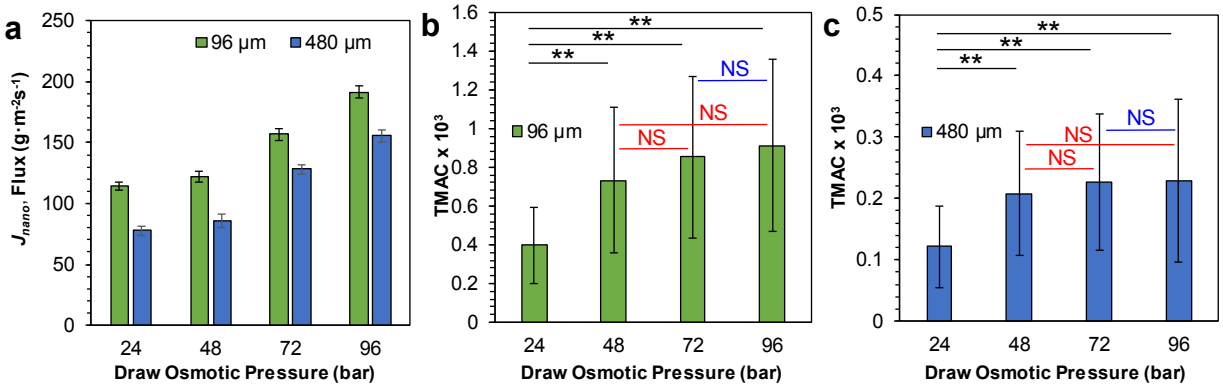

Figure 4: ***(a)*** *Plot comparing the estimated flux in the vapor-trap as a function of osmotic pressure for FTS-coated vapor-traps of l_h = 96 µm and 480 µm. TMAC for vapor-trap of* ***(b)*** *l_h = 96 µm and* ***(c)*** *480 µm. The TMAC is of the order of 10^{-4} – 10^{-3}, indicative of specular reflection and the variation of TMAC with osmotic pressure is found to saturate to a constant value and is statistically not significant (*NS *with p > 0.2) beyond an osmotic pressure of 48 bar for both l_h =*

*96 μm and 480 μm; (** indicates $p < 0.05$). Statistical significance was estimated using one-way ANOVA followed by Tukey's post-hoc HSD test. Error bars represent ± s.d. from the mean.*

The maximum flux for vapor pressure driven evaporation between two opposing feed and draw menisci of varying osmotic pressure is commonly described using the Herz hypothesis.[13] For the tested draw concentration, a theoretical maximum flux of 120 $g \cdot m^{-2} \cdot s^{-1}$ (1 M draw), 181 $g \cdot m^{-2} \cdot s^{-1}$ (1.5 M draw), and 241 $g \cdot m^{-2} \cdot s^{-1}$ (2 M draw) is estimated using Hertz hypothesis[13] and is comparable in magnitude to the experimentally reported flux in Figure 4a. It is worth noting that recent numerical[17, 46-47] and experimental studies[18] have questioned the validity of Hertz hypothesis as the hypothesis discards the effects of extended meniscus[47] and non-equilibrium local effects[17] at nanoscale confinements and potentially underpredict the overall evaporation flux.

Vapor trap operation at various osmotic pressures

Since J_{nano} was measured using an optical method dependent on the intensity of the monitoring dye (Figure 5); therefore, a control experiment was required to ensure that reduction in draw microchannel dye intensity was not a consequence of photobleaching. Consequently, a device without a vapor-trap (control case) was filled with Rb, followed by monitoring the Rb intensity for 20 min (same duration of time as used for estimating J_{nano} with the vapor trap). No reduction in Rb intensity was observed during the entire experiment (Figure 5a). Subsequently with the vapor trap in place, osmotic pressure of draw was increased from 24 bar (0.5 M) to 96 bar (2 M) and net draw dilution (Figure S6 for fluorescence time-lapse images) was recorded and plotted for FTS-coated vapor-traps of l_h = 96 μm and 480 μm (Figure 5b–e). Figure 5a shows representative draw dilution images for l_h = 96 μm, and 480 μm respectively, when draw osmotic concentration was fixed to 1 M.

As a general trend, for a given osmotic gradient, the time necessary to achieve a 50% dilution in the draw was faster for nanochannels with l_h = 96 μm in comparison to l_h = 480 μm. When the draw concentration was 0.5 M (Figure 5b), 50% dilution was achieved faster by 6 min in the nanochannel with l_h = 96 μm in comparison to 480 μm. With increase in draw concentration to 1 M, the time necessary to achieve a 50% dilution (Figure 2) due to condensation of water was 3.2 min (l_h = 96 μm, Figure 5c) and 5.7 min (l_h = 480 μm, Figure 5c). Similarly, at t = 10 min, percent dilution of 81.5%, 67.1%, was observed in the draw for l_h = 96 μm, and 480 μm respectively. For the maximum draw concentration of 2 M (Figure 5e), 50% dilution was achieved faster by 30 s in nanochannel with l_h = 96 μm (2 min) in comparison to 480 μm (1 min

30 s). Similarly, for the OTS-modified nanochannels, a 50% dilution in draw concentration (Figure S7) was observed to be faster by 26% nanochannels with l_h = 203 µm (2.8 min) in comparison to channels with l_h = 595 µm (3.8 min) implying a non-linear scaling of transmission resistance for vapor phase transport of water molecules inside the hydrophobic vapor-trap.

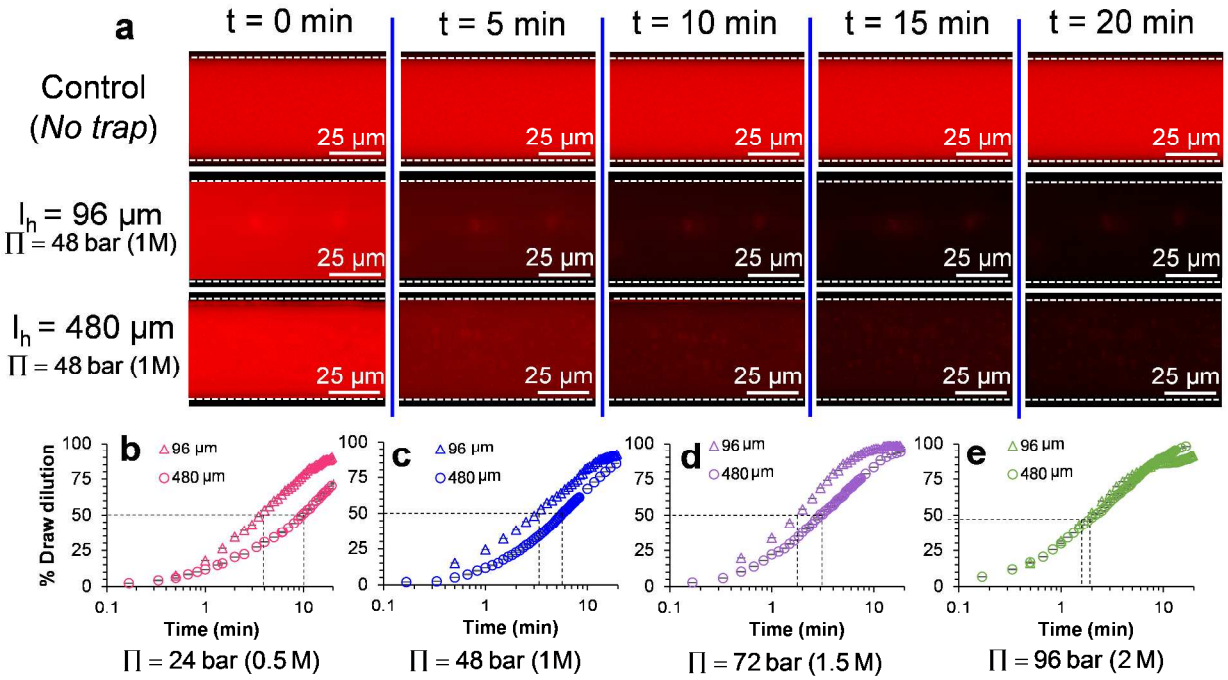

Figure 5: ***(a)*** *Images capturing reduction in Rhodamine B intensity in draw microchannel as a function of time for vapor-trap for a control case with no vapor-trap in contrast to devices with* l_h *= 96 µm and 480 µm. Plots comparing draw dilution as a function of time for FTS vapor-traps of length 96 µm and 480 µm for a draw concentration of* ***(b)*** *0.5 M* ***(c)*** *1 M* ***(d)*** *1.5 M and,* ***(e)*** *2 M. When the draw concentration was 2M, 50% dilution was achieved faster by 30 s in nanochannel with* l_h *= 96 µm in comparison to 480 µm. However, when the draw concentration was 0.5 M, 50% dilution was achieved faster by 6 min in nanochannel with* l_h *= 96 µm in comparison to 480 µm demonstrating that vapor transport is dependent on the pressure gradient between draw and feed. Error bars represent ± s.d. from the mean.*

Treatment of high salinity 3 M shale flowback water

Filtration of high-salinity (brine) solutions such as those arising during hydraulic fracturing for shale excavation pose extreme challenges for treatment using existing technology.[48] The concentrations of these solutions often exceed 3 M or 180,000 ppm and are composed of heavy

metals, in addition to possessing several potentially toxic and radioactive constituents, biocides, and organics. Such high-salinity solutions pose significant difficulties to pre-filter for treatment using wastewater treatment plants.[48] Flow back water is commonly disposed *via* underground injection wells[48] that are at sub-surface depths of 800 – 13,000 feet with potential correlations to enhanced seismic activities.[49]

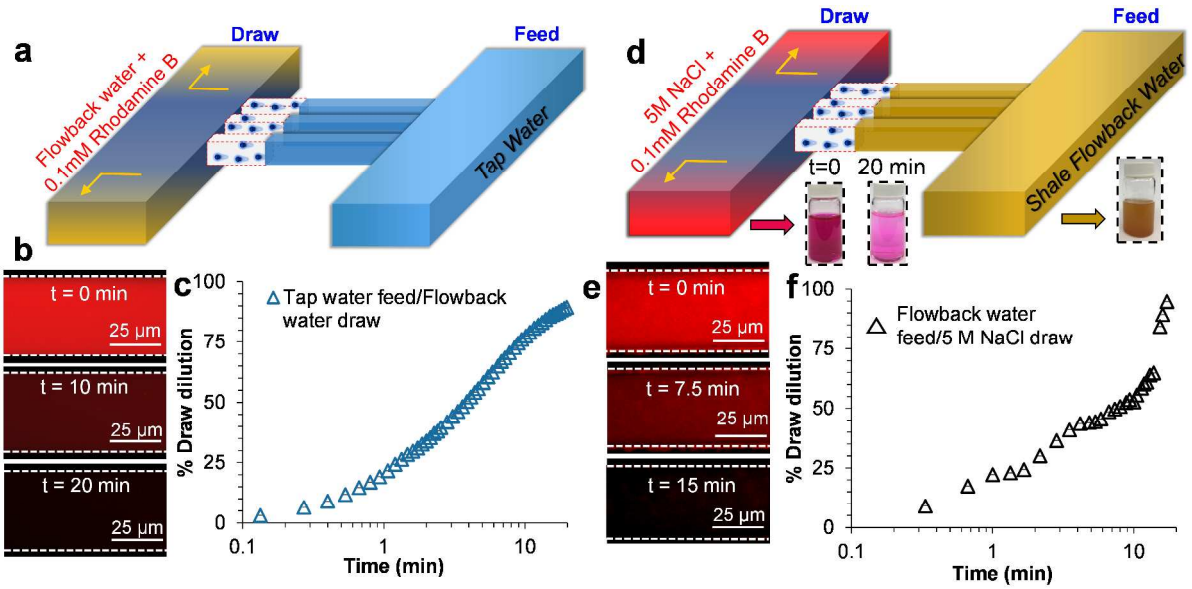

*Figure 6: **Shale flowback water as draw.** **(a)** Schematic depicting Utica shale flowback water, tagged with 0.1mM Rb as draw, and tap water (300 ppm) as feed. **(b)** Desalting of draw resulting in **(c)** dilution of flowback waters over 20 min. **Shale flowback water as feed.** **(d)** Schematic depicting desalting of Utica Shale water with a relative molarity of 3M as feed and 5 M NaCl tagged with 0.1mM Rhodamine B as draw. Inset shows photo of raw flowback water from Utica shale well. The developed present device resisted wetting of Utica shale water and demonstrated a 95% reduction in **(e)** NaCl draw intensity without fouling. **(f)** Plot showing dilution of draw with the incoming water from Utica produced water feed.*

A proof-of-concept demonstration for treatment of raw shale flowback water from the Utica shales (184,000 ppm or 3 M) *via* osmotic distillation was evaluated. First, the flowback water was pre-filtered thrice using a 20 µm sized coffee filter to remove large particulates and introduced to the draw, separated from a tap water (300 ppm) feed by a nanochannel with FTS-coating and l_h = 480 µm. Condensation of water-vapor from higher vapor pressure feed into the draw resulted in ~92% desalting of shale flowback water feed over 20 min (Figure 6b, c). The tap water serves as a simulated low concentration waste stream that can be readily available as domestic wastewater (gray water) or agricultural run-off which are either discarded to local water bodies or piped to municipal wastewater treatment facilities.[50] Use of the shale water as a draw

solution can therefore be beneficial in diluting the shale water stream (without adding further contaminants) before secondary treatment by conventional means.

Next, Utica shale flowback water was introduced into the feed (Figure 6d) and a 5 M NaCl tagged with 0.1 mM Rhodamine B dye was introduced in the draw to potentially extract usable water from the shale flowback solution. Such a scenario may arise when other highly concentrated industrial wastewaters are available and cannot be easily treated.[48] Condensation of water vapor from the shale flowback water feed was recovered in draw as observed by a reduction in Rb intensity (Figure 6e). At 20 min, the salt concentration had decreased by about 95%, that is from 5 M to 0.25 M (Figure 6f). Importantly, the high-salinity flowback water was used as feed over three separate runs and draw desalting of 95% was observed repeatedly, demonstrating re-usability and resistance to fouling within the same vapor trap.

High Flux separation of trace amounts of toluene and chloroform from water *via* pervaporation

Another key issue in flow backwater disposal is the presence of trace organics. It is known that produced water from both Marcellus and Barnett shale reserves contain volatile aromatic hydrocarbons including toluene and are filtered using filtration techniques such as pervaporation.[51] Inefficient separation leaves residual organics, which upon release pose a risk of contamination to source surface and groundwater. In traditional pervaporation, a hydrophobic membrane first separates a non-polar solute (permeate) from an aqueous solvent and the separated permeate is subsequently collected *via* vaporization. The rate of extraction of permeate is referred to as permeate flux and traditional pervaporation membranes report a permeate flux of 0.03 – 0.3 $g \cdot m^{-2} s^{-1}$. However, during this separation, a fraction of water invariably leaks into the membrane constituting the leakage flux, and previous reports have shown that the leakage flux is similar in magnitude to the permeate flux, thereby demonstration poor separation efficiency.[52-53]

As another proof-of-concept demonstration, toluene tagged with 0.1 mg/ml of Nile Red (NR) dye ($\lambda_{ex}/\lambda_{em}$ = *552/636 nm, insoluble in water)* was diluted 200 times in water and placed on the reservoir connecting hydrophobic draw microchannel (Figure 7a) to simulate conditions of trace toluene in water. Under lack of an external driving pump, the tagged toluene immediately separated from the water due to capillarity and filled both the hydrophobic microchannel and nanochannels as observed by strong fluorescence signal (Figure 7b, c). This fluorescence intensity was within 1% of intensity registered when the microfluidic-nanofluidic system was calibrated with 100% toluene (NR tagged) without any water,

demonstrating a filtration efficiency of ~99% (Figure 7d). Similar observations were seen with 200 times diluted chloroform (Figure 7b).

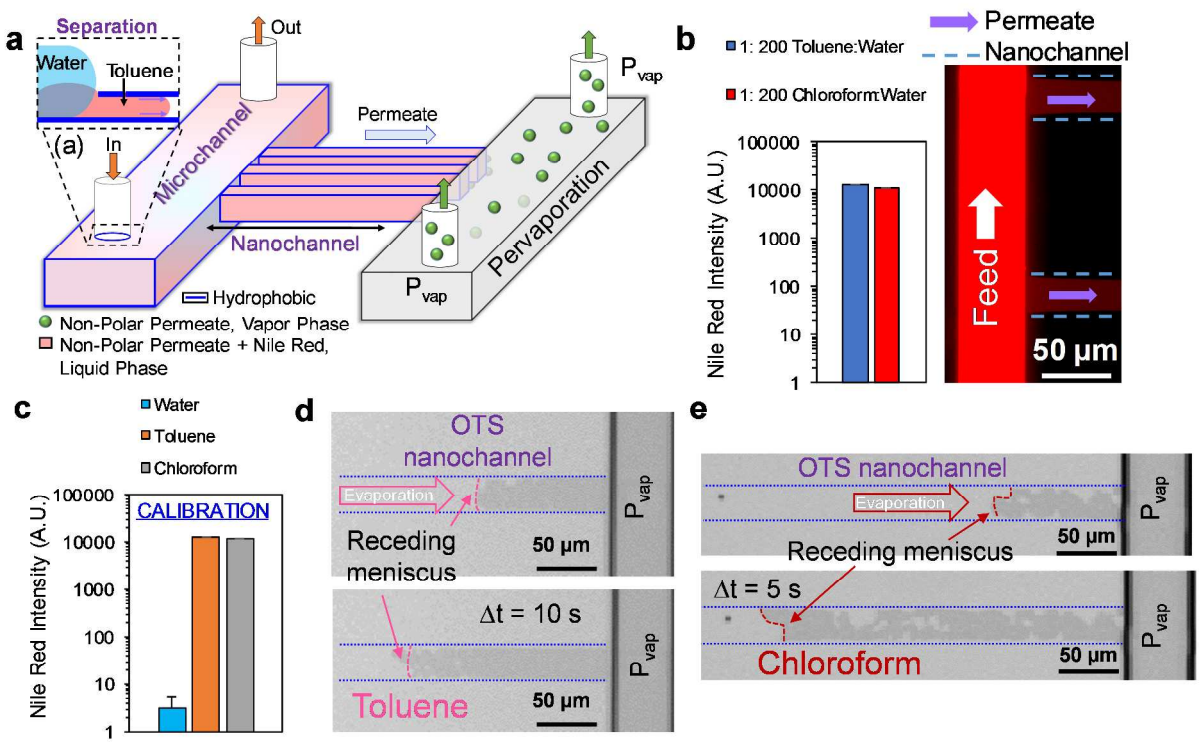

*Figure 7: (**a**) Working principle of a pervaporation setup. Inset: The solvents display an affinity to wet the hydrophobic microchannel as opposed to liquid water (highlighted in blue outline) and consequently toluene/chloroform separates from the mixture to wet both the hydrophobic microchannel and nanochannel due to capillarity. (**b**) Measured intensity inside nanochannel when 0.5 µl of toluene tagged with 0.1 mg/ml Nile red (NR, a non-polar soluble dye) mixed with 100 µl water (200x dilution) was introduced in draw. Fluorescence image shows the filtered toluene from 200x water, filling both the hydrophobic microchannel and nanochannel. Observations were similar when tested with chloroform. (**c**) Calibrated intensity of NR tagged toluene/chloroform inside the microchannel, introduced without dilution with water. Water, a polar-solvent does not mix with NR and exhibits negligible intensity inside the nanochannel. Measured NR intensity with 200x dilution (Figure 7b), and in Figure 7c without dilution, was within 1%, indicating minimal water leakage compared to state-of-the-art pervaporation membranes. Evaporation induced receding meniscus of (**d**) toluene and (**e**) chloroform permeate inside OTS coated nanochannel was recorded via time-lapse imaging for 90 s. Representative micrograph shows local receding meniscus position inside nanochannel. Rate of change of permeate volume was converted to mass flux by multiplying with the density of the respective solvent. Dashed lines are eye guides for nanochannel.*

Upon conducting the intensity measurement, the device was continuously monitored visually by a microscope and the draw microchannel consisting of the separated toluene or /chloroform was first evacuated by connecting the draw reservoir to a vacuum pump. Once the draw microchannel was emptied (monitored visually using microscope), the pump was immediately switched off, leaving the separated permeate (in liquid phase) inside the entirety of nanochannel. The permeat-side solvent then gradually begins to evaporate from the nanochannel to the ambient at atmospheric pressure, driven by the solvent vapor pressure. While the evacuated permeate was not collected, the mass flux of this evaporating permeate (toluene or chloroform) inside the hydrophobic (OTS or FTS) nanochannel was estimated by tracking the evaporation induced receding meniscus[18] as a function of time (Figure 7d, e).

An average flux of 8.88 $g \cdot m^{-2}s^{-1}$ (OTS vapor trap) and 12.5 $g \cdot m^{-2}s^{-1}$ (FTS vapor trap) was measured for toluene (Figure 7d); 38.3 $g \cdot m^{-2}s^{-1}$ (OTS vapor trap) and 48 $g \cdot m^{-2}s^{-1}$ (FTS vapor trap) was measured for chloroform (Figure 7e). Increased mass flux for chloroform was expected due to a higher vapor pressure (29.5 kPa) in comparison to toluene (3.8 kPa) at 25°C. Whereas, increased flux for both toluene and chloroform for FTS nanochannels, compared to OTS functionalization is a consequence of higher surface wettability of the two solvents with OTS. The bulk contact angle measured was ~5° for both solvents in OTS, in contrast to 55.6°, 38° for toluene, chloroform respectively in FTS. Previous molecular dynamic simulations showed that line tension of solvents at the three-phase contact line increases with improved surface wettability,[54] indicating higher line tension for solvents on OTS nanochannels here. Equilibrium pervaporation flux, hence is governed by competing effects of line tension versus vapor pressure at the evaporating permeate meniscus, the quantification of which is beyond the scope of the present work. The enhancement in flux is in contrast to traditional pervaporation membranes without well-defined (i.e., randomly distributed) porous networks that show linear increase in transmission resistance with increases membrane thickness unlike non-linear scaling observed for two-phase transport inside the vapor-trap.[52-53]

Summary and Conclusions

In summary, investigation of water vapor transport across hydrophobic patches of varying lengths was carried out to estimate the tangential momentum accommodation coefficient for water vapor hydrophobic surface interaction. A surface modification process was carried out to pattern either (heptadecafluoro-1,1,2,2-tetrahydrodecyl)trichlorosilane (FTS) with fluoro or n-Octadecyltrichlorosilane (OTS) with methyl terminal groups. Optical characterization using a fluorescence measurement was used to determine a measured flux of water, which was then used

with unified slip model to compute the tangential momentum accommodation coefficient. For FTS coated nanochannels, extracted TMAC varied between 0.1 – 1 x 10^{-3}, and between 0.1 – 0.4 x 10^{-3} for OTS coated nanochannels. Low values of TMAC ($O(10^{-4} – 10^{-3})$) observed here is indicative of near-elastic collisions of water molecules with nanochannel surfaces permitting enhanced flux by drastically minimizing transmission resistance to water vapor transport. Two potential demonstrations are reported for future applications of this work: (a) Treat Utica shale flow back water either as draw or feed *via* osmotic distillation, and (b) Separate of 200x diluted toluene and chloroform from water, governed by pervaporation at a flux ~$O(10^{1})$ $g \cdot m^{-2} \cdot s^{-1}$, which is significantly higher than traditional pervaporation membranes.

Estimation of TMAC provides another design parameter for membrane developers for engineering new materials and subsequently design and fabricate arrays of hydrophobic conduits, that exhibits enhanced flux for scale-up in practical osmotic or membrane distillation applications. The reported results point to the importance of molecule-surface interactions in determining overall vapor phase flux, which when taken into account may help to engineer next-generation membranes or separation systems with enhanced flux and minimal transmission resistance.

Materials and Methods

Lithography

The microchannels and nanochannels were patterned in borosilicate cover glass using standard ultraviolet (UV) lithography followed by wet etching with hydrofluoric acid or HF (1:4, HF: H_2O, for microchannels). Following a second photolithography step,[26] a buffered oxide etch (BOE) with 10:1 BOE (J.T. Baker Inc.) was used to etch the nanochannels to achieve a depth of 80 nm using methods reported previously.[26] Devices were sealed using a soda lime microscope slide (Fisher Scientific) as a cover with pre-drilled access holes and bonded to the etched channel layer using calcium-assisted low temperature (65°C for 1h, 115°C for 2h) bonding technique.[26]

Surface Modification

Our team has also reported surface functionalization recipes for glass substrates previously.[28, 36] Briefly, the bonded devices (Figure 1a) were first flushed with DI water, followed by flushing twice with ethanol and once with anhydrous toluene (Sigma Aldrich, St. Louis, MO). Each device was then dried in a vacuum desiccator at a pressure of 30 mTorr for 30 min and inspected under a microscope to visually ensure dry devices. Next, inside a continuously dry nitrogen purged glove bag, a 0.5% v/v of either heptadecafluoro-1,1,2,2-tetrahydrodecyl)trichlorosilane (FTS, Gelest Inc.) or n-Octadecyltrichlorosilane

(OTS, Gelest Inc.) in anhydrous toluene was used to functionalize the silica walls with either a fluoro-terminated or methyl-terminated silane monolayer.[28, 55] After a time Δt_f, the solvents were pumped out from the microchannels, following which the device was removed from the glove bag and placed inside the vacuum desiccator at a pressure of 30 mTorr for 60 min to completely dry out the channels. Next, the device was flushed twice with toluene and once with N,N-dimethylformamide, DMF (Sigma Aldrich, St. Louis, MO) to remove any physisorbed silane layers. Finally, DMF was removed from nanochannel device by placing inside the vacuum desiccator for 30 min, followed by annealing at 80°C on a hot plate for 45 min.

Flux Estimation

A transient convection-diffusion model was solved in COMSOL Multiphysics (v5.3) to estimate the velocity of condensing water, u_m in draw microchannel, contributing to the observed reduction in dye intensity (Figure S8). The use of convection-diffusion equations to estimate flux correlated from the dilution of a dye follows from well-established demonstration inside microfluidic platforms in the past.[56-57] Mass conservation between water vapor transport through the nanoscale vapor-trap and net convective flux in the draw (calculated from convection-diffusion model, supplementary information) was then used to estimate nanoscale flux of water vapor, J_{nano}.

Conflicts of Interest

The authors do not have conflicts of interest to declare.

Acknowledgements

The authors acknowledge the staff at Nanotech West Laboratories at The Ohio State University for assistance with equipment during fabrication and characterization of devices, Ohio Supercomputer for providing computational resources. Prof. David Cole's group is acknowledged for providing shale flowback water samples, and also for assistance in ion-chromatography measurements. The authors would like to acknowledge partial financial support from the National Science Foundation (NSF) through grant CBET-1335946 and the U.S. Department of Energy through grant number: DE-FE0024357, and The Office of Energy and Environment at The Ohio State University. K.K. Rangharajan acknowledges The Ohio State University for a presidential fellowship.

References

1. M. A. Celia, P. C. Reeves and L. A. Ferrand, *Rev. Geophys.*, 1995, **33**, 1049-1057.
2. D. Rana and T. Matsuura, *Chem. Rev.*, 2010, **110**, 2448-2471.
3. J. A. Prince, G. Singh, D. Rana, T. Matsuura, V. Anbharasi and T. S. Shanmugasundaram, *J. Membr. Sci.*, 2012, **397-398**, 80-86.

4. A. Sorrentino, G. Gorrasi and V. Vittoria, *Trends Food Sci. Technol.*, 2007, **18**, 84-95.
5. M. Stoppa and A. Chiolerio, *Sensors*, 2014, **14**, 11957.
6. A. Gunther and K. F. Jensen, *Lab Chip*, 2006, **6**, 1487-1503.
7. A. P. Straub, N. Y. Yip, S. Lin, J. Lee and M. Elimelech, *Nat. Energy*, 2016, **1**, 16090.
8. A. Alkhudhiri, N. Darwish and N. Hilal, *Desalination*, 2012, **287**, 2-18.
9. P. Wang and T.-S. Chung, *J. Membr. Sci.*, 2015, **474**, 39-56.
10. H. B. Park, J. Kamcev, L. M. Robeson, M. Elimelech and B. D. Freeman, *Science*, 2017, **356**.
11. T. Humplik, J. Lee, S. O'Hern, T. Laoui, R. Karnik and E. N. Wang, *Nanotechnol.*, 2017, **28**, 505703.
12. E. B. Arkilic, K. S. Breuer and M. A. Schmidt, *J. Fluid Mech.*, 2001, **437**, 29-43.
13. J. Lee, T. Laoui and R. Karnik, *Nat. Nanotechnol.*, 2014, **9**, 317-323.
14. M. Fuest, C. Boone, K. K. Rangharajan, A. T. Conlisk and S. Prakash, *Nano Lett.*, 2015, **15**, 2365–2371.
15. J. K. Holt, H. G. Park, Y. Wang, M. Stadermann, A. B. Artyukhin, C. P. Grigoropoulos, A. Noy and O. Bakajin, *Science*, 2006, **312**, 1034-1037.
16. M. Majumder, N. Chopra, R. Andrews and B. J. Hinds, *Nature*, 2005, **438**, 44.
17. Z. Lu, S. Narayanan and E. N. Wang, *Langmuir*, 2015, **31**, 9817-9824.
18. Y. Li, M. A. Alibakhshi, Y. Zhao and C. Duan, *Nano Lett.*, 2017, **17**, 4813-4819.
19. G. Karniadakis, A. Beskok and N. Aluru, *Microflows and nanoflows: Fundamentals and simulation.*, Springer, New York, 2005.
20. J. C. Maxwell, *Philos. Trans. R. Soc. London*, 1879, **170**, 231-256.
21. W. Lei and D. R. McKenzie, *J. Phys. Chem. C*, 2015, **119**, 22072-22079.
22. O. V. Sazhin, S. F. Borisov and F. Sharipov, *J. Vac. Sci. Technol. A*, 2001, **19**, 2499-2503.
23. I. A. Graur, P. Perrier, W. Ghozlani and J. G. Méolans, *Phys. Fluids*, 2009, **21**, 102004.
24. H. Yamaguchi, T. Hanawa, O. Yamamoto, Y. Matsuda, Y. Egami and T. Niimi, *Microfluid. Nanofluid.*, 2011, **11**, 57-64.
25. R. Karnik, K. Castelino, C. Duan and A. Majumdar, *Nano Lett.*, 2006, **6**, 1735-1740.
26. M. Pinti, T. Kambham, B. Wang and S. Prakash, *J. Nanotechnol. Eng. Med.*, 2013, **4**, 020905.
27. T.M. Long, S. Prakash, M.A. Shannon and J.S. Moore, *Langmuir*, 2006, **22**, 4104-4109.
28. S. Prakash, T.M. Long, J.C. Selby, J.S. Moore and M.A. Shannon, *Anal. Chem.*, 2007, **79**, 1661-1667
29. S. Flink, F.C.J.M. van Veggel and D.N. Reinhoudt, *J. Phys. Org. Chem.*, 2001, **14**, 407-415.
30. N. R. Tas, J. Haneveld, H. V. Jansen, M. Elwenspoek and A. v. d. Berg, *Appl. Phys. Lett.*, 2004, **85**, 3274-3276.
31. S. J. Wierzchowski and D. A. Kofke, *J. Phys. Chem. B*, 2003, **107**, 12808-12813.
32. W. H. Fissell, A. T. Conlisk, S. Datta, J. M. Magistrelli, J. T. Glass, A. J. Fleischman and S. Roy, *Microfluid. Nanofluid.*, 2011, **10**, 425-433.
33. A. Beskok and G. E. Karniadakis, *Microscale Thermophysical Engineering*, 1999, **3**, 43-77.
34. G. A. Bird, *Annu. Rev. Fluid Mech.*, 1978, **10**, 11-31.
35. N. Dongari, A. Agrawal and A. Agrawal, *Int. J. Heat Mass Transfer*, 2007, **50**, 3411-3421.
36. K. K. Rangharajan, K. J. Kwak, A. T. Conlisk, Y. Wu and S. Prakash, *Soft Matter*, 2015, **11**, 5214-5223.
37. G.W. Finger, J.S. Kapat and A. Bhattacharya, *J. Fluids Eng.*, 2006, **129**, 31-39.
38. J. A. K. Howard, V. J. Hoy, D. O'Hagan and G. T. Smith, *Tetrahedron*, 1996, **52**, 12613-12622.

39. Y. Wu, S. Misra, M. B. Karacor, S. Prakash and M. A. Shannon, *Langmuir*, 2010, **26**, 16963-16972.
40. S. Joseph and N. R. Aluru, *Nano Lett.*, 2008, **8**, 452-458.
41. M. E. McGovern, K. M. R. Kallury and M. Thompson, *Langmuir*, 1994, **10**, 3607-3614.
42. Y. Wang and M. Lieberman, *Langmuir*, 2003, **19**, 1159-1167.
43. C. Cottin-Bizonne, J.-L. Barrat, L. Bocquet and E. Charlaix, *Nat. Mater.*, 2003, **2**, 237.
44. J. S. Babu and S. P. Sathian, *J. Chem. Phys.*, 2011, **134**, 194509.
45. J. L. Plawsky, M. Ojha, A. Chatterjee and P. C. Wayner, *Chem. Eng. Commun.*, 2008, **196**, 658-696.
46. R. Holyst, M. Litniewski and D. Jakubczyk, *Soft Matter*, 2015, **11**, 7201-7206.
47. S. Narayanan, A. G. Fedorov and Y. K. Joshi, *Langmuir*, 2011, **27**, 10666-10676.
48. D. L. Shaffer, L. H. Arias Chavez, M. Ben-Sasson, S. Romero-Vargas Castrillón, N. Y. Yip and M. Elimelech, *Environ. Sci. Technol.*, 2013, **47**, 9569-9583.
49. F. R. Walsh and M. D. Zoback, *Sci. Adv.*, 2015, **1**, E1500195.
50. E. Eriksson, K. Auffarth, M. Henze and A. Ledin, *Urban Water*, 2002, **4**, 85-104.
51. S. J. Maguire-Boyle and A. R. Barron, *Environ. Sci.: Processes Impacts*, 2014, **16**, 2237-2248.
52. S. Schnabel, P. Moulin, Q. T. Nguyen, D. Roizard and P. Aptel, *J. Membr. Sci.*, 1998, **142**, 129-141.
53. I. Shams and H. R. Mortaheb, *Desalin. Water Treat.*, 2016, **57**, 6852-6862.
54. J. H. Weijs, A. Marchand, B. Andreotti, D. Lohse and J. H. Snoeijer, *Phys. Fluids,* 2011, **23**, 022001.
55. S. Prakash, T. M. Long, J. C. Selby, J. S. Moore and M. A. Shannon, *Anal. Chem.*, 2007, **79**, 1661-1667.
56. R. F. Ismagilov, A. D. Stroock, P. J. A. Kenis, G. Whitesides and H. A. Stone, *Appl. Phys. Lett.*, 2000, **76**, 2376-2378.
57. Y. Du, J. Shim, M. Vidula, M. J. Hancock, E. Lo, B. G. Chung, J. T. Borenstein, M. Khabiry, D. M. Cropek and A. Khademhosseini, *Lab Chip*, 2009, **9**, 761-767.

Table of Contents Entry

Transmission resistance for selective water vapor permeation through hydrophobic conduits with varying degree of surface wettability is estimated inside a nanofluidic device.

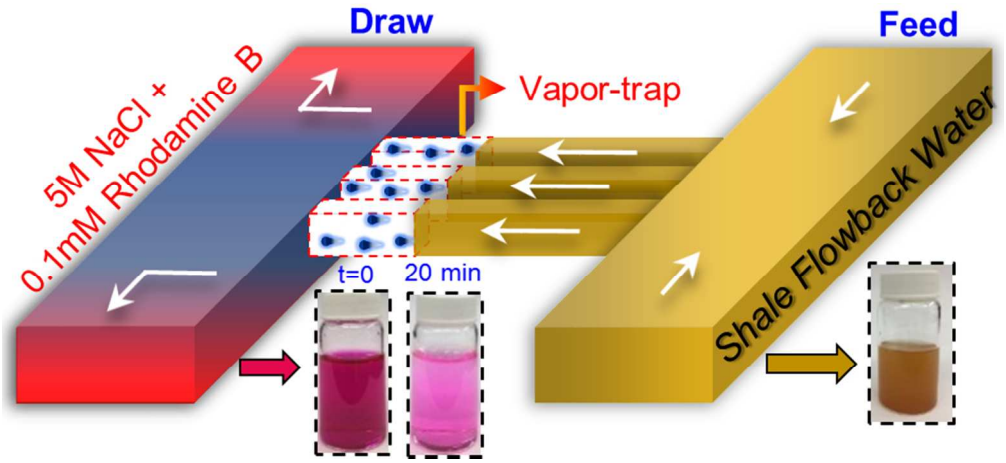

80x36mm (300 x 300 DPI)